Electronic supplementary information

Multiple-state interfacial electron injection competes with excited state relaxation and de-excitation to determine external quantum efficiencies of organic dye-sensitized solar cells

Min Zhang, Lin Yang, Cancan Yan, Wentao Ma and Peng Wang*

State Key Laboratory of Polymer Physics and Chemistry, Changchun Institute of Applied Chemistry, Chinese Academy of Sciences, Changchun, 130022, China

*Corresponding Author, Email: peng.wang@ciac.ac.cn; Telephone: 0086-431-85262952

Table of contents

1. Synthesis of **C265** S3

1.1. Materials S3

1.2. Synthetic procedures S3

2. Analyses on the anchor dependent energy levels and absorption spectra: BA vs CA S4

3. Details of the target analysis method S5

4. Reference S5

5. Additional data S6

1 Synthesis of C265

1.1 Materials

Dimethyl formamide and phosphorus oxychloride were distilled before use. 4-(7-(4,4-Dihexyl-4*H*-cyclopenta[1,2-*b*:5,4-*b*′]dithiophen-2-yl)benzo[*c*][1,2,5]thiadiazol-4-yl)-*N*,*N*-bis(4-(hexyloxy)phenyl)aniline (**1**) was synthesized in our previous paper.[S1] Other chemicals are purchased from Sigma-Aldrich and used without further purification.

1.2 Synthetic procedures

Scheme S1 Synthetic route of **C265**[a]

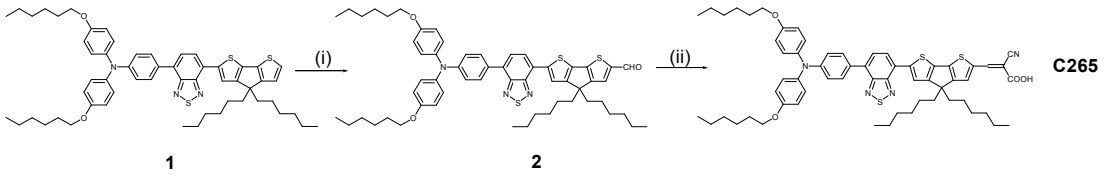

[a] Reagents and conditions: (i) DMF, $POCl_3$, DCE, 0 °C to 40 °C, 10 h; (ii) cyanoacetic acid, piperidine, $CHCl_3$, reflux, 12 h.

The synthetic route of **C265** is illustrated in Scheme S1, and the preparation details are described as follows.

6-(7-(4-(Bis(4-(hexyloxy)phenyl)amino)phenyl)benzo[*c*][1,2,5]thiadiazol-4-yl)-4,4-dihexyl-4*H*-cyclopenta[1,2-*b*:5,4-*b*′]dithiophene-2-carbaldehyde (2). In a three-necked round bottom flask was dissolved **1** (0.340 g, 0.368 mmol) in dichloromethane (10 mL) and cooled to 0 °C using an ice salt bath. DMF (0.142 mL, 1.841 mmol) and $POCl_3$ (0.041 mL, 0.442 mmol) was added to the reaction mixture. The resulting solution was stirred at 40 °C for 10 h. Saturated sodium acetate aqueous solution (10 mL) was added and the mixture was stirred for another 2 h. Then the mixture was extracted into dichloromethane, and the organic layer was washed with water and dried over anhydrous sodium sulfate. After removing solvent under reduced pressure, the residue was purified by column chromatography (toluene/petroleum ether 60–90 °C, 1/3, *v*/*v*) on silica gel to yield a purple powder as the desired product **2** (0.298 g, 85% yield). ^{1}H NMR (400 MHz, $CDCl_3$) δ: 9.85 (s, 1H), 8.05 (s, 1H), 7.92 (d, *J*=7.6 Hz, 1H), 7.83 (d, *J*=8.8 Hz, 2H), 7.65 (d, *J*=7.6 Hz, 1H), 7.59 (s, 1H), 7.12 (d, *J*=8.8 Hz, 4H), 7.04 (d, *J*=8.8 Hz, 2H), 6.85 (d, *J*=8.8 Hz, 4H), 3.94 (t, *J*=6.4 Hz, 4H), 1.96 (m, 4H), 1.78 (m, 4H), 1.47 (m, 4H), 1.35 (m, 8H), 1.16 (m, 12H), 1.05 (m, 4H), 0.91 (m, 6H), 0.80 (m, 6H). ^{13}C NMR (100 MHz, $CDCl_3$) δ: 182.35, 162.95, 158.21, 155.80, 153.90, 152.49, 149.14, 147.62, 144.48, 143.60, 140.10, 136.64, 132.85, 129.80, 129.67, 128.17, 127.03, 126.45, 125.48, 125.19, 121.32, 119.39, 115.29, 68.19, 54.15, 37.67, 31.53, 29.57, 29.26, 25.69, 24.58, 22.54, 13.97. MS (ESI) *m*/*z* calcd. for ($C_{58}H_{69}N_3O_3S_3$): 951.45. Found: 952.46 ($[M+H]^+$). Anal. calcd. for $C_{58}H_{69}N_3O_3S_3$: C, 73.15; H, 7.30; N, 4.41. Found: C, 73.22; H, 7.27; N, 4.38.

3-(6-(7-(4-(Bis(4-(hexyloxy)phenyl)amino)phenyl)benzo[*c*][1,2,5]thiadiazol-4-yl)-4,4-dihexyl-4*H*-cyclopenta[1,2-*b*:5,4-*b*′]dithiophen-2-yl)-2-cyanoacrylic acid (C265). To a stirred solution of **2** (0.280 g, 0.294 mmol) and cyanoacetic acid (75 mg, 0.883 mmol) in chloroform was added piperidine (0.203 mL, 2.058 mmol). The reaction mixture was refluxed under argon for 12 h and then acidified

with 2 M hydrochloric acid aqueous solution. The crude product was extracted into chloroform, washed with water, and dried over anhydrous sodium sulfate. After removing the solvent under reduced pressure, the crude product was purified by column chromatography (chloroform/methanol, 10/1, *v*/*v*) on silica gel to yield a black powder as the desired product **C265** (0.243 g, 81% yield). ^{1}H NMR (400 MHz, THF-d_8) δ: 8.40 (s, 1H), 8.25 (s, 1H), 7.99 (s, 1H), 7.89 (s, 2H), 7.82 (s, 1H), 7.70 (s, 1H), 7.08 (d, *J*=8.0 Hz, 4H), 6.97 (d, *J*=8.0 Hz, 2H), 6.85 (d, *J*=8.0 Hz, 4H), 3.94 (t, *J*=6.0 Hz, 4H), 2.05 (m, 4H), 1.75 (m, 4H), 1.49 (m, 4H), 1.29 (m, 24H), 0.92 (m, 6H), 0.80 (m, 6H). ^{13}C NMR (100 MHz, THF-d_8) δ: 163.64, 159.36, 156.83, 154.55, 153.26, 149.93, 148.65, 146.88, 145.79, 141.01, 140.68, 137.81, 133.29, 131.71, 130.46, 129.38, 129.06, 127.62, 126.92, 126.14, 125.88, 122.28, 119.98, 117.33, 115.88, 68.59, 54.82, 38.45, 34.43, 32.65, 32.39, 32.34, 30.86, 30.43, 30.12, 27.82, 27.42, 26.55, 23.33, 14.23. HR-MS (MALDI) *m*/*z* calcd. for ($C_{61}H_{70}N_4O_4S_3$): 1018.45592. Found: 1018.45617. Anal. calcd. for $C_{61}H_{70}N_4O_4S_3$: C, 71.87; H, 6.92; N, 5.50. Found: C, 71.89; H, 6.93; N, 5.48.

2 Analyses on the anchor dependent energy levels and absorption spectra: BA vs CA

The influence of anchors on the energy levels was first inspected by measuring cyclic voltammograms (Fig. S1a) of the dye solutions in THF to reckon the highest occupied molecular orbital (HOMO) and lowest unoccupied molecular orbital (LUMO) energy levels as tabulated in Table S1. The **C265** dye with the more electron-deficient anchor CA presents an obviously lower LUMO (−3.41 eV vs vacuum) and a comparable HOMO (−5.05 eV vs vacuum), compared to **C257** characteristic of the BA anchor (LUMO: −3.18 eV; HOMO: −5.04 eV). This remarkably depressed LUMO brings forths an energy-gap shrinkage for **C265** with respect to **C257**. The impact of anchors on the light harvesting capacity was preliminarily examined at the molecular level by recording the electronic absorption spectra of **C257** and **C265** dissolved in THF. As depicted in Fig. S1b, **C265** presents overlapped absorption bands, which can be separated into two individual bands via multi-peak Gaussian fitting (Fig. S2). The latter band is centered at 554 nm, which is red-shifted by 18 nm with respect to that of 536 nm for **C257**. Moreover, the molar absorption coefficient at the maximum absorption wavelength is augmented from 40.8 to 49.7×10^3 M^{-1} cm^{-1} along with the anchor variation from BA to CA.

We further resorted to quantum calculation to gain insight into the anchor dependent energy levels and absorption spectra. As listed in Table S1, our DFT calculations can nicely simulate the relative alignments of HOMOs and LUMOs of these two dyes. The obviously lower LUMO for **C265** with respect to that of **C257** can be ascribed to the more electron-deficient characteristic of CA (LUMO: −2.32 eV) in comparison with BA (LUMO: −1.45 eV). The distinct influences of anchors on HOMO and LUMO can be understood with a view on the molecular configurations, showing that both anchors in these two dyes are far away from the triphenylamine electron-donor. The time dependent density functional theory (TDDFT) calculations can mimic the absorption spectra of these two dyes very well. The calculated absorption wavelengths (λ_{abs}^{calc}), oscillator strengths (*f*), and transition assignments are also collected in Table S1. In general, the absorption bands in the visible region are originated from the $S_0 \rightarrow S_1$ and $S_0 \rightarrow S_2$ transitions. The $S_0 \rightarrow S_1$ absorption bands for both **C257** and **C265** are mainly attributed to the transitions from HOMO and HOMO−1 to LUMO. Of special interest, the contribution from HOMO is obviously reduced for **C265** (61%) with respect to that of 85% for **C257**. Further

analysis on the corresponding molecular orbital distributions (Fig. S3) reveal that the replacement of BA with CA makes the HOMO be mainly localized on the triphenylamine unit, and the LUMO on the BT, CPDT and CA segments, indicating a smaller overlap between HOMO and LUMO. It can be concluded that the evidently reduced HOMO/LUMO energy-gap of **C265** dominates its red-shifted low-energy absorption peak with respect to **C257**. In addition, the absorption bands due to $S_0 \rightarrow S_2$ transition for both dyes are mainly originated from HOMO−1 to LUMO and HOMO to LUMO+1.

3 Details of the target analysis method

The analysis of the fs-TA data was performed with the global and target analysis program GLOTARAN (http://glotaran.org/). The singular value decomposition (SVD) of the data was carried out to determine the starting number of components which were involved in interfacial electron injection processes. Resorting to the global analysis with a sequential kinetic model, the number of components was further optimized. Meanwhile, the main lifetimes and the evolution-associated difference spectra (EADS) of each component were also obtained. Due to the very small instrument response function, the first component decays with the first lifetime. The second of the EADS is formed with the first lifetime and decays with the second lifetime, and so on. The EADS derived from global analysis are considered to the weighted sum (with only positive contributions) of SADS. Then, to determine the detailed kinetic parameters of each photophysical process related to the electron injection, the target analysis with a kinetic model was employed to fit the time-resolved data. Only one kinetic parameter was optimized at a time. Three criteria were used to estimate the quality of the aforementioned fitting results: i) the sum of square of errors should be the lowest; ii) the singular vectors derived from the SVD of residual matrix should show no significant residual structure; iii) the original data should be overlaid with the fitted traces.

4 Reference

S1 M. Zhang, Y. Wang, M. Xu, W. Ma, R. Li and P. Wang, *Energy Environ. Sci.*, 2013, **6**, 2944–2949.

5 Additional data

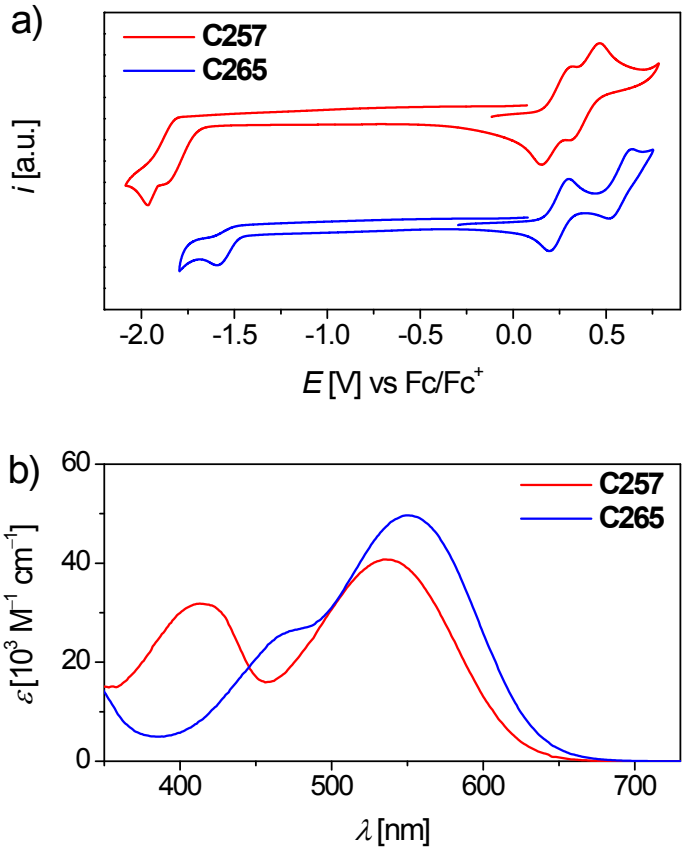

Fig. S1 (a) Cyclic voltammograms of **C257** and C**265** in THF with 0.1 M EMITFSI as the supporting electrolyte. Working electrode: glassy carbon; scan rate: 5 mV s^{-1}. (b) Molar extinction coefficients (ε) plotted as a function of wavelength (λ) for the THF solutions of **C257** and **C265**.

Table S1 Measured and calculated energy levels, energy-gaps, and electronic absorption properties of **C257** and **C265**

Dye	$\mathbf{E}_{H}$ [eV] [a]	$\mathbf{E}_{L}$ [eV] [a]	$\mathbf{E}_{H-1}$ [eV] [b]	$\mathbf{E}_{H}$ [eV] [b]	$\mathbf{E}_{L}$ [eV] [b]	$\mathbf{E}_{L+1}$ [eV] [b]	$\Delta\mathbf{E}_{H/L}$ [eV] [b]	$\Delta\mathbf{E}_{H-1/L}$ [eV] [b]	$\Delta\mathbf{E}_{H/L+1}$ [eV] [b]	λ_{abs}^{meas} [nm] [c]	ε_{abs}^{meas} [10^3 M^{-1} cm^{-1}] [c]	λ_{abs}^{cacl} [nm] [d]	f [d]	Transition [d]
C257	–5.04	–3.18	–5.61	–5.16	–2.69	–2.01	2.47	2.92	3.15	413	31.8	392	0.28	H−1→L (48%) H→L+1 (30%)
										536	40.8	505	1.58	H→L (85%) H−1→L (12%)
C265	–5.05	–3.41	–5.86	–5.26	–3.00	–2.43	2.26	2.86	2.83	462	20.1	420	0.20	H−1→L (33%) H→L+1 (43%)
										554	49.7	522	1.89	H→L (61%) H−1→L (31%)

[a] Measured frontier orbital energies with respect to vacuum were estimated via $\mathbf{E} = -4.88 - eE_{onset}$, where E_{onset} is the onset potential (Fig. S1a) of oxidation and reduction of the ground state of a dye measured with cyclic voltammetry. H and L represent HOMO and LUMO, respectively;

[b] Frontier orbital energies with respect to vacuum were calculated at the PBE0/6-311G(d,p) level of theory for a dye in THF;

[c] λ_{abs}^{meas} and ε_{abs}^{meas} were measured for a dye in THF, and the values of **C265** were obtained via multi-peak Gaussian fitting as presented in Fig. S2;

[d] λ_{abs}^{cacl}, oscillator strength (*f*), and corresponding transition assignments were derived from calculations at the TD-CAM-B3LYP/6-311G(d,p) level of theory for a dye in THF.

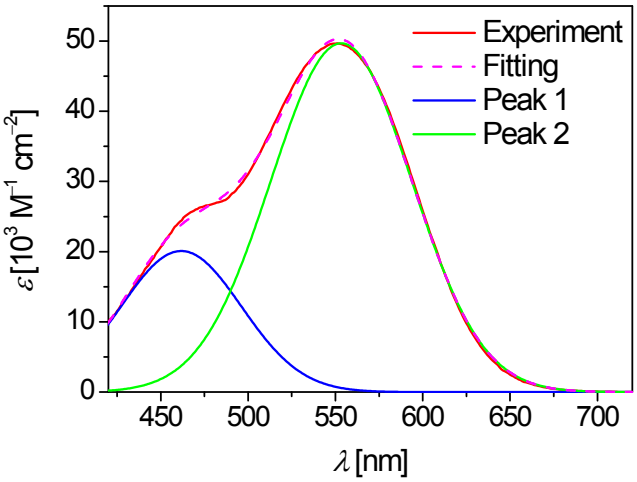

Fig. S2 Electronic absorption spectra of the **C265** dye dissolved in THF. The multi-peak Gaussian fitting nicely reproduces the measured electronic absorption spectrum and distinctly affords multiple absorption bands with clear peaks in the visible light region.

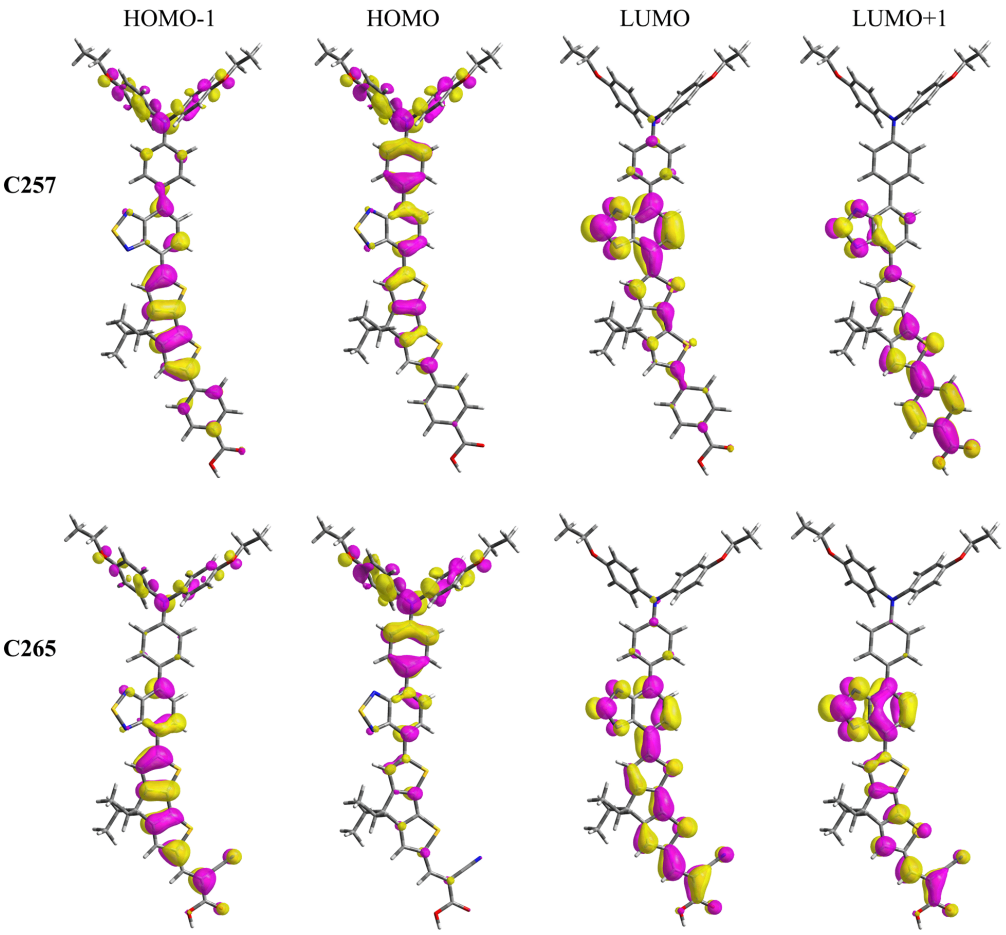

Fig. S3 The distributions of $S_0 \rightarrow S_1$ and $S_0 \rightarrow S_2$ transition involved frontier molecular orbitals. The isodensity surface values are fixed at 0.03.

Table S2 Measured and calculated electronic absorption/photoluminescence properties of **C257** and **C265** in contact with the acetonitrile-based iodine electrolyte

Dye	λ_{max}^{abs} [nm] [a]	λ_{max}^{PL} [nm] [a]	Stokes shift [eV] [a]	λ_{max}^{abs} [nm] [b]	f^{abs} [c]	Transition [c]	λ_{max}^{PL} [nm] [b]	f^{PL} [d]	Transition [d]	Stokes shift [eV] [b]
C257	519	701	0.62	503	1.57	H→L (85%) H–1→L (12%)	705	1.66	L→H (100%)	0.70
C265	524	728	0.66	520	1.90	H→L (60%) H–1→L (31%)	747	2.23	L→H (93%)	0.72

[a] Measured maximum absorption (λ_{max}^{abs}), maximum PL (λ_{max}^{PL}), and Stokes shift of a dye-grafted titania film and further immersed in the acetonitrile-based electrolyte;

[b] Calculated maximum absorption (λ_{max}^{abs}), maximum PL (λ_{max}^{PL}), and Stokes shift at the TD-CAM-B3LYP/6-311G(d,p) level of theory for a dye dissolved in acetonitrile;

[c] Oscillator strength (f^{abs}) and transition assignment were derived from the TDDFT calculations on electronic absorption spectra;

[d] Oscillator strength (f^{PL}) and transition assignment were derived from the TDDFT calculations on photoluminescence spectra.

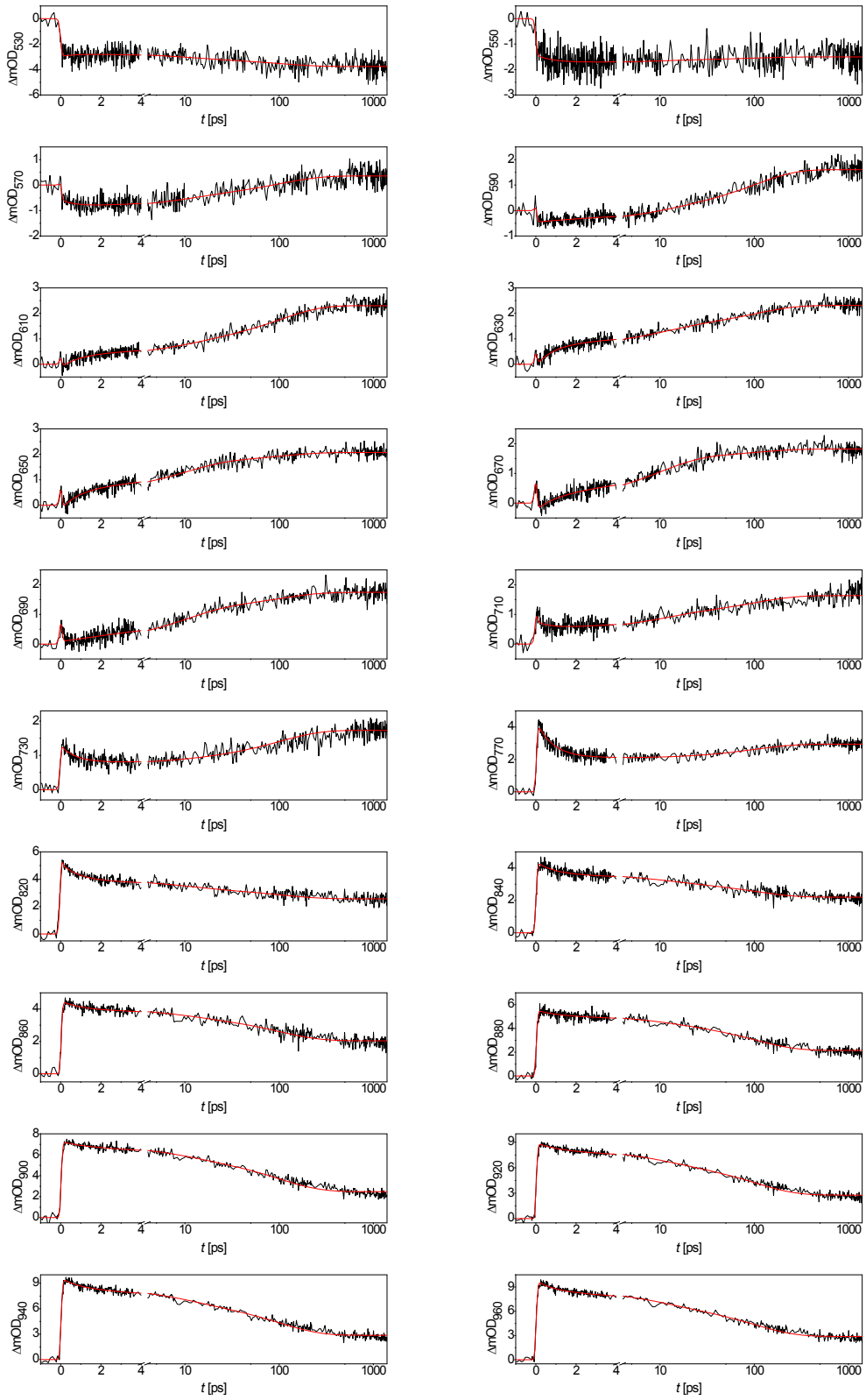

Fig. S4 Selected kinetic traces (black) at different wavelengths for a 2.1-µm-thick titania film grafted with **C257** and immersed in a realistic iodine electrolyte. The red lines are fittings obtained from target analysis.

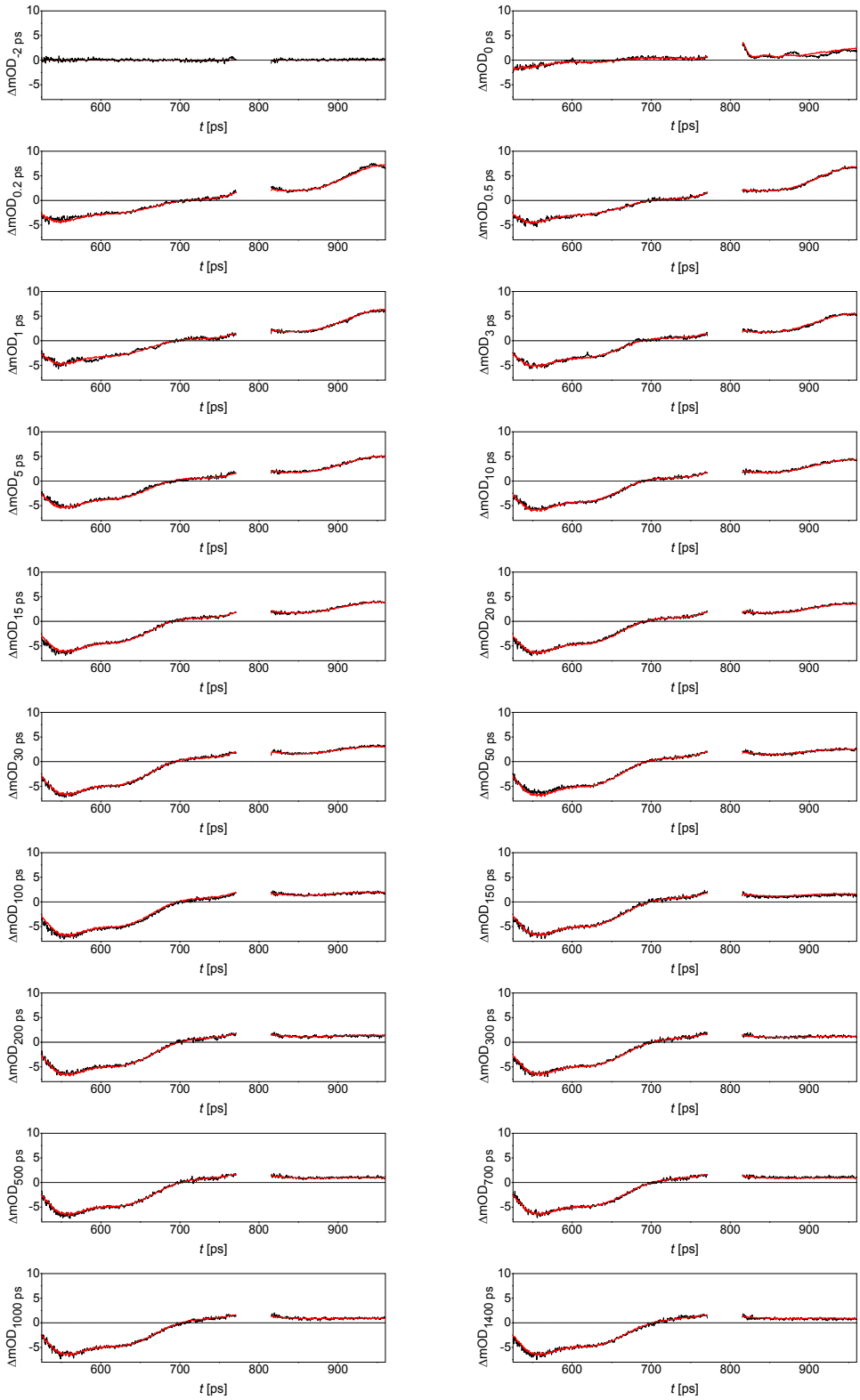

Fig. S5 Selected TA spectra (black) at different time delays for a 2.1-µm-thick titania film grafted with **C257** and immersed in a realistic iodine electrolyte. The red lines are fittings obtained from target analysis.

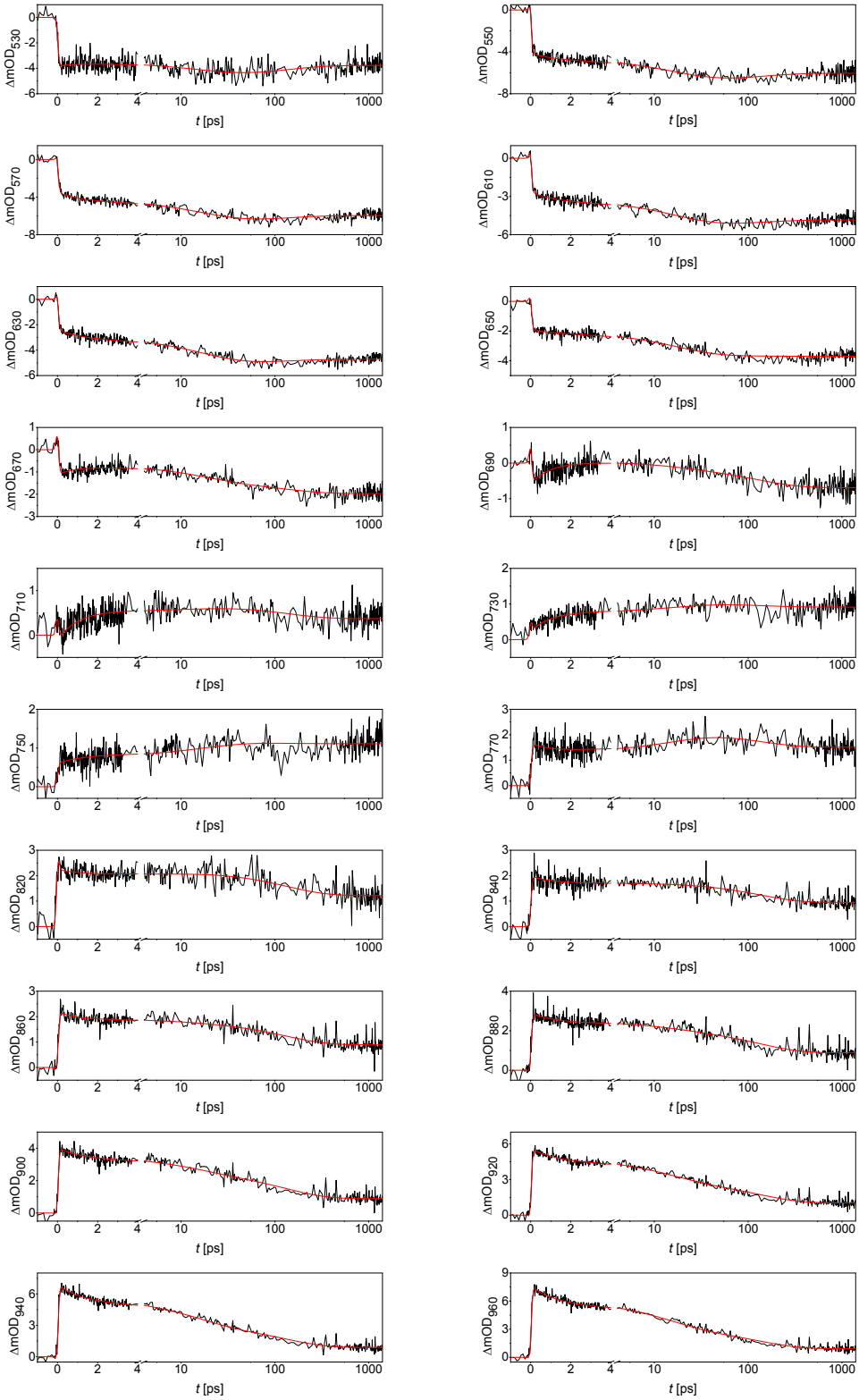

Fig. S6 Selected kinetic traces (black) at different wavelengths for a 2.1-µm-thick titania film grafted with **C265** and immersed in a realistic iodine electrolyte. The red lines are fittings obtained from target analysis.

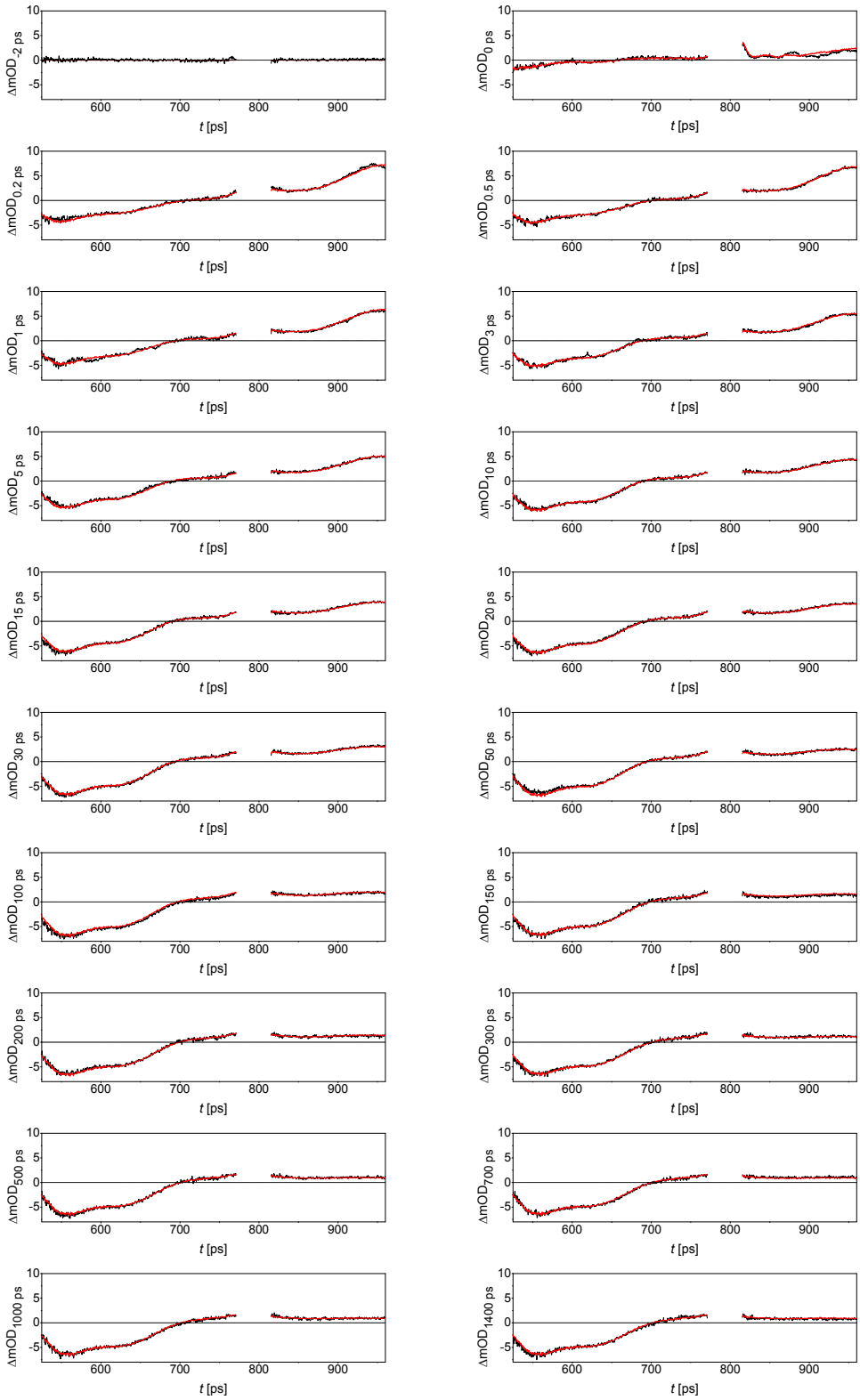

Fig. S7 Selected TA spectra (black) at different time delays for a 2.1-µm-thick titania film grafted with **C265** and immersed in a realistic iodine electrolyte. The red lines are fittings obtained from target analysis.

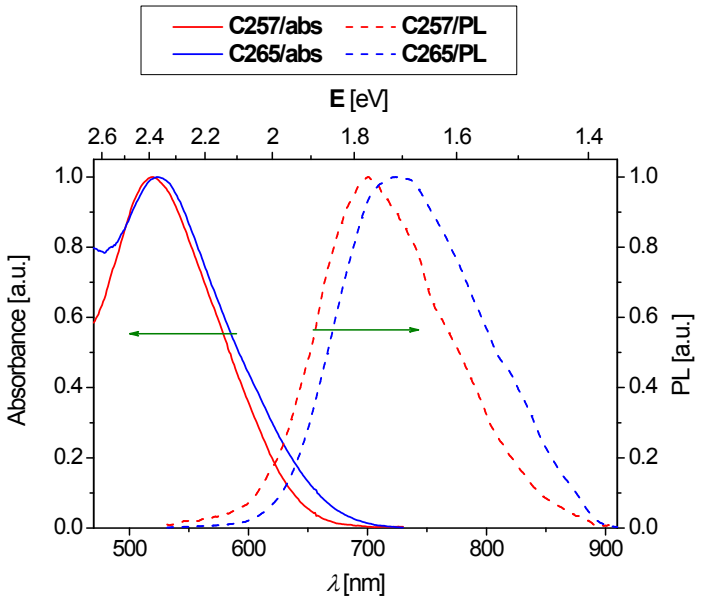

Fig. S8 Normalized electronic absorption spectra (solid lines) and PL spectra (dash lines) of **C257** and **C265** grafted titania films immersed in a realistic iodine electrolyte. The absorption of a titania film has been subtracted for clarity of presentation. The PL spectra recorded with an ICCD camera are excited with 490 nm laser.

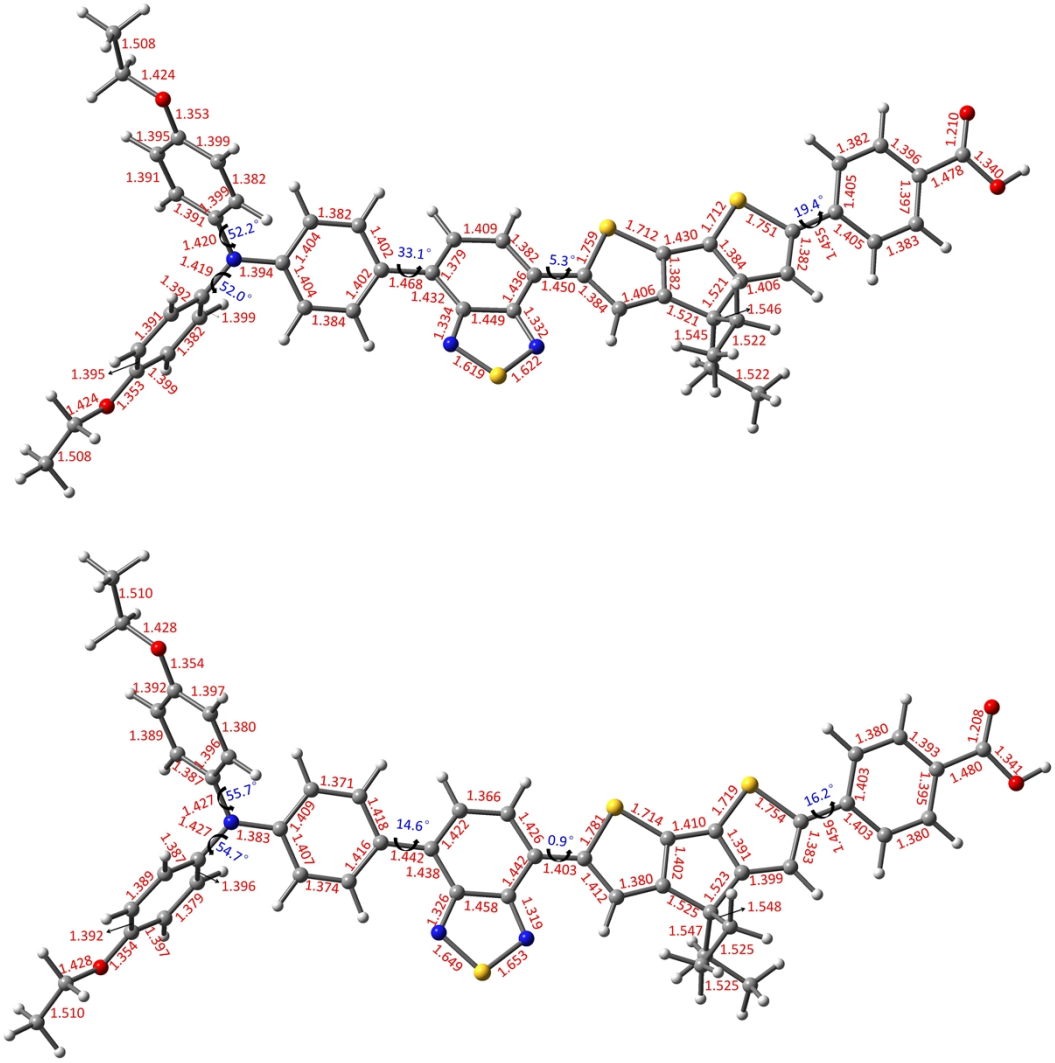

Fig. S9 Optimized geometries of the ground state (S_0, top) and lowest singlet excited state (S_1, bottom) of **C257** in acetonitrile at the PBE0/6-31G(d,p) and TD-CAM-B3LYP/6-31G(d,p) levels, respectively. The hexyl groups were reduced to ethyl.

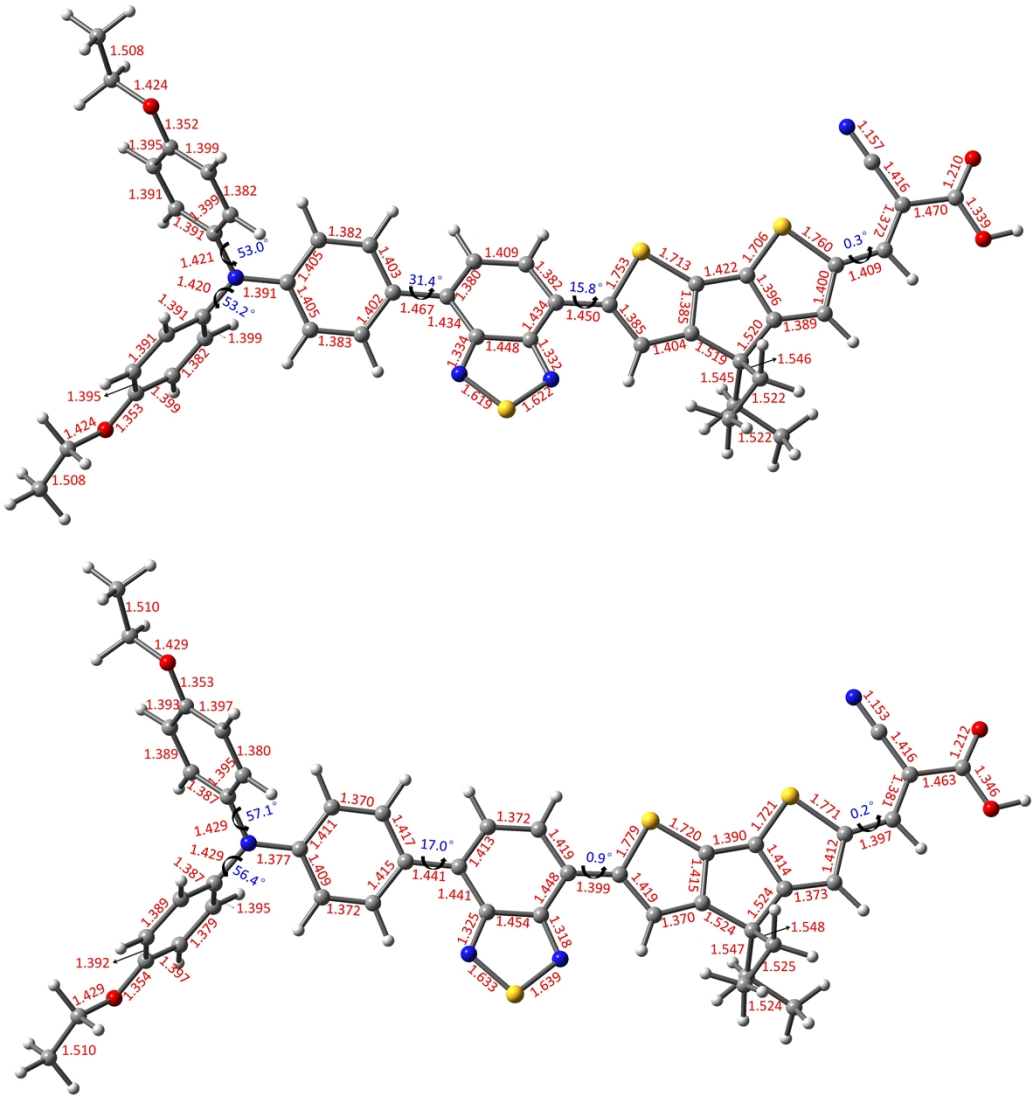

Fig. S10 Optimized geometries of the ground state S_0 (top) and lowest singlet excited state S_1 (bottom) of **C265** in acetonitrile at the PBE0/6-31G(d,p) and TD-CAM-B3LYP/6-31G(d,p) levels, respectively. The hexyl groups were reduced to ethyl.

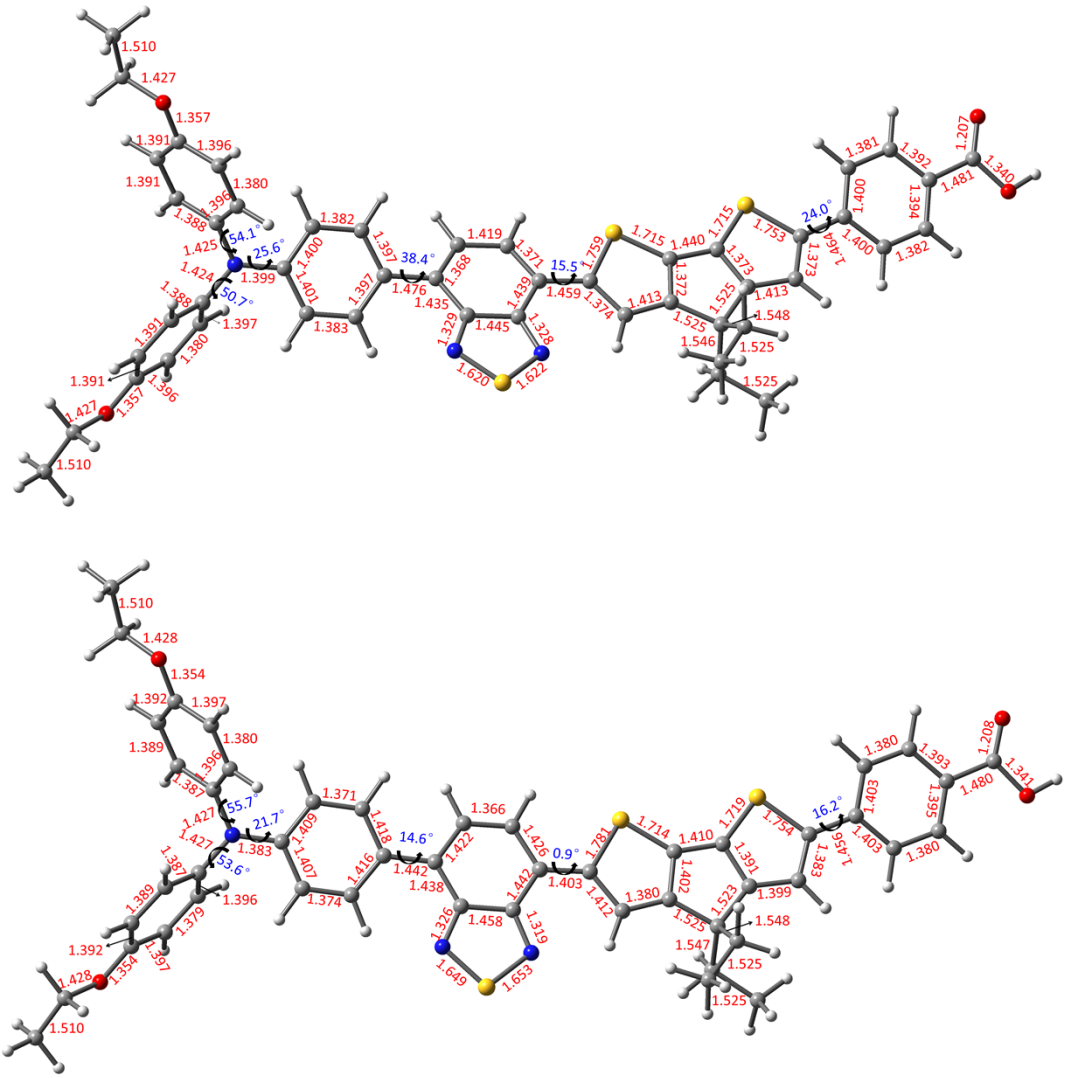

Fig. S11 Optimized geometries of the ground state (S_0, top) and lowest singlet excited state (S_1, bottom) of **C257** in acetonitrile at the CAM-B3LYP/6-311G(d,p) and TD-CAM-B3LYP/6-311G(d,p) levels, respectively. The hexyl groups were reduced to ethyl.

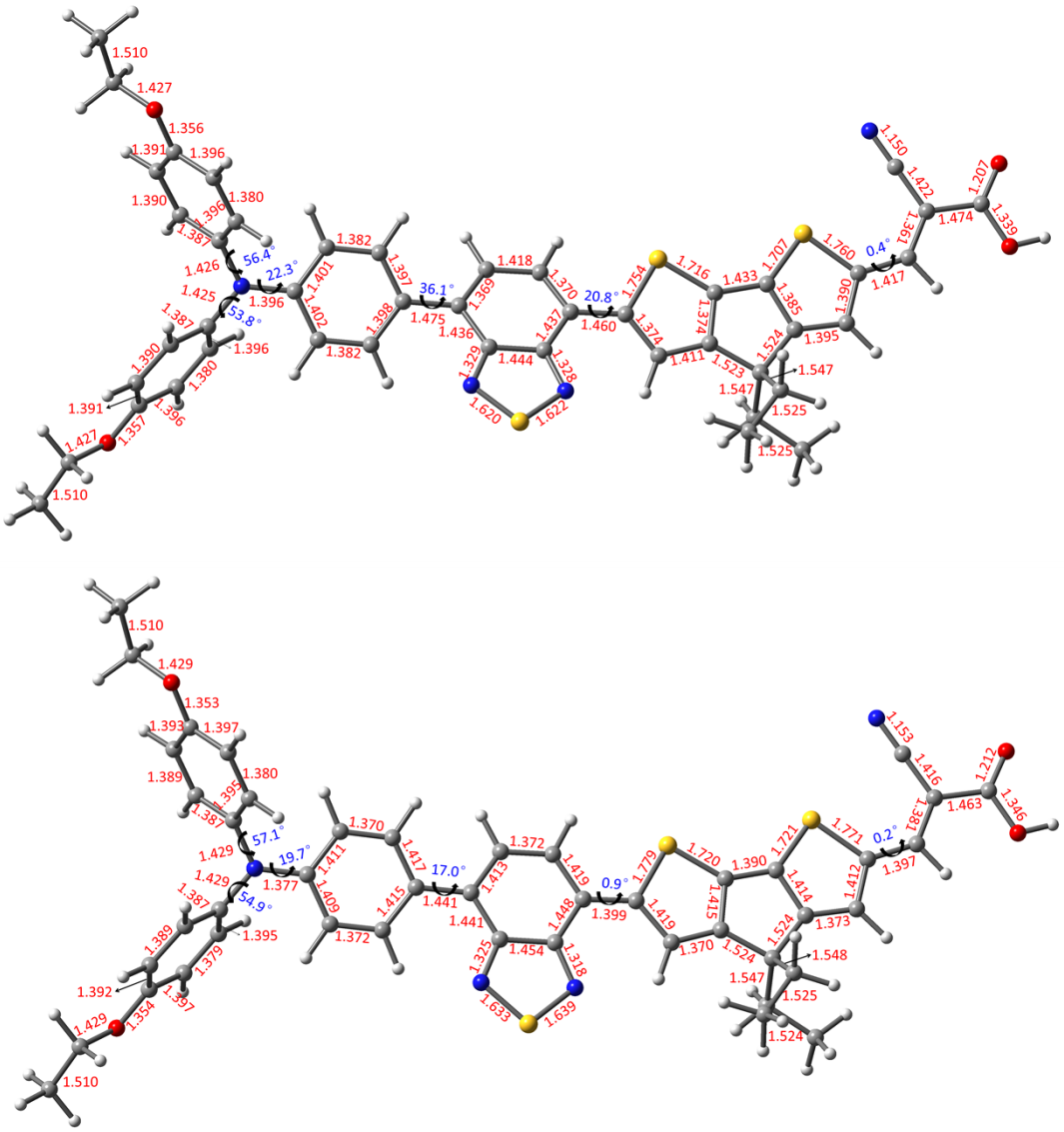

Fig. S12 Optimized geometries of the ground state S_0 (top) and lowest singlet excited state S_1 (bottom) of **C265** in acetonitrile at the CAM-B3LYP/6-311G(d,p) and TD-CAM-B3LYP/6-311G(d,p) levels, respectively. The hexyl groups were reduced to ethyl.

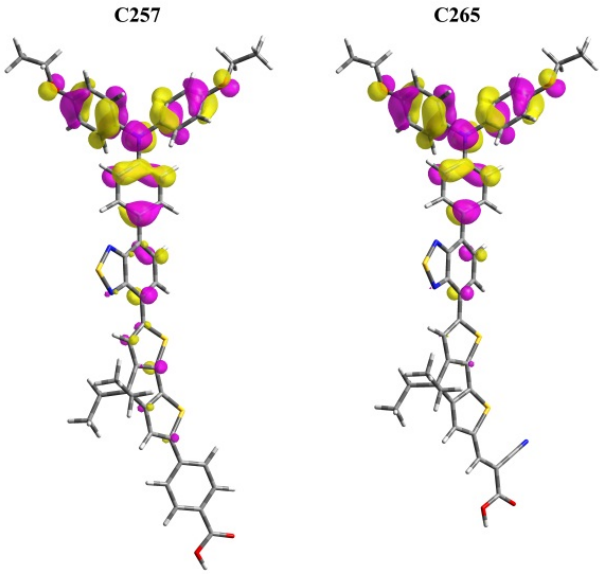

Fig. S13 The distribution of holes in the photooxidized dye molecules with acetonitrile as the solvent, which were calculated at the UPBE0/6-311G(d,p) level.

Table S3 Averaged photovoltaic parameters of four cells measured at an irradiance of 100 mW cm^{-2}, simulated AM1.5 sunlight [a)]

Dye	J_{sc}^{EQE} [mA cm^{-2}]	J_{sc} [mA cm^{-2}]	V_{oc} [mV]	FF	PCE [%]
C257	15.74±0.11	16.00±0.13	774±5	0.702±0.005	8.7±0.2
C265	11.38±0.14	11.64±0.15	694±4	0.726±0.004	5.9±0.1

[a)] J_{sc}^{EQE} is derived via wavelength integration of the product of the standard AM1.5 emission spectrum (ASTM G173-03) and the EQEs measured at the short-circuit. The validness of measured photovoltaic parameters is evaluated by comparing the calculated J_{sc}^{EQE} with the experimentally measured J_{sc}.